ZnO microwire lasing generated by mid-infrared laser pulses of various polarization

Yu Liu,[1] Yang Wang,[1] Jingying Xiao,[1] Pengzuo Jiang,[1] Song Luo,[2] Zhanghai Chen,[2] Liang-You Peng ®,[1,3,4,5]
Yunquan Liu,[1,3,4,5] Qihuang Gong,[1,3,4,5] and Chengyin Wu ®[1,3,4,5,*]

[1]*State Key Laboratory for Mesoscopic Physics and Frontiers Science Center for Nano-optoelectronics, School of Physics,*
Peking University, Beijing 100871, China
[2]*Department of Physics, College of Physical Science and Technology, Xiamen University, Xiamen 361005, China*
[3]*Collaborative Innovation Center of Quantum Matter, Beijing 100871, China*
[4]*Collaborative Innovation Center of Extreme Optics, Shanxi University, Taiyuan, Shanxi 030006, China*
[5]*Peking University Yangtze Delta Institute of Optoelectronics, Nantong, Jiangsu 226010, China*

ZnO nanowire (NW) lasing driven by mid-infrared (MIR) laser pulses has attracted significant attention owing to its remarkable wavelength-independent lasing threshold and potential applications in diverse situations. However, the properties of MIR laser-driven ZnO microwire (MW) lasing are rarely studied when the wire diameter is increased from nanoscale to microscale, comparable to the wavelength of the driving laser. Here we experimentally measured the ZnO MW lasing driven by MIR laser with different polarizations. The measurements show that the laser polarized along the c axis was more efficient for the lasing in MW with diameter smaller than the driving laser wavelength, while the polarization dependence was ambiguous when the MW diameter was greater than the driving laser wavelength. Through the modeling of the lasing process in ZnO MW, the observed polarization dependence is reproduced and can be attributed to the combined effect of the optical interference of the driving laser in the MW and the varying absorption properties of different MWs. The former is related to the MW diameter and the latter is sensitive to the sample growth condition. Our findings shed light on the feasibility of manipulation of the ZnO MW lasing.

DOI: 10.1103/PhysRevB.109.245307

I. INTRODUCTION

ZnO microstructures have attracted considerable attention in the fields of electronics, optics, optoelectronics, and biological imaging owing to their facile chemical growth method, compact size, diverse physical and optical properties, and multiple control degrees of freedom [1]. Among them, one-dimensional (1D) microwire (MW) and nanowire (NW) are particularly interesting because of their capabilities for low-threshold lasing [2,3], given that stimulated emission in ZnO can be optically pumped [4]. Moreover, 1D ZnO MW possesses a natural high-Q factor microcavity formed by its hexagonal side surface, rendering its use as a microlasing element, *in situ* ultraviolet (UV) light source, functional elements in on-chip optics and integrated photonic circuits feasible [5,6]. To date, ZnO MW lasing pumped by lasers with near-resonant or above-band-gap photon energy ($\geqslant 3.37$ eV) have been achieved and widely investigated [7–10]. However, the UV pump laser has restricted the application of these studies in integrated photonics due to strong UV absorption of the circuit materials [11–13]. Increasing the pump wavelength not only overcomes the problem, but also facilitates separating the lasing signal from the pump laser, taking advantage of their wavelength difference. Therefore, extending the pump wavelength toward longer wavelength has long been an unattained research goal [14–19].

In pursuit of longer pump wavelengths, lasing pumped by intense mid-infrared (MIR) laser was achieved in ZnO NW via strong-field tunneling excitation and demonstrated the independence of the lasing threshold from the MIR pump wavelength [19]. The wavelength-independent feature significantly relaxes the restriction on the pump field. Thus, ZnO NW lasing pumped by MIR laser is promising for various applications and attracting increasing interest. By further increasing the size of the target, lasing via six-photon up-conversion in ZnO MW was demonstrated, exhibiting nonperturbative behaviors in the high pump intensity regime [18]. However, control of MIR-laser-pumped ZnO MW lasing has rarely been studied. Several alternative parameters may exert control on the optically pumped micro/nanostructure lasing, such as the employment of various sample morphologies and changing pump polarization to achieve spatial and temporal customization of the lasing [1], alteration of the dominant lasing mode via size-related spatial hole burning [20] or resonant condition [21], switching the gain process via the pulse width of the pump laser [22], utilization of the local enhancement effect of surface plasmons [23], or optical suppression of the field-driven recombination process [24]. Among these, the size of the MW and polarization of the pump laser are the most fundamental parameters to be investigated. They may significantly modulate the lasing yield and threshold, as indicated by an experiment on MW lasing pumped by a UV laser [25], wherein the pump polarization dependence originated from anisotropic effective reflectivity and polarization-dependent
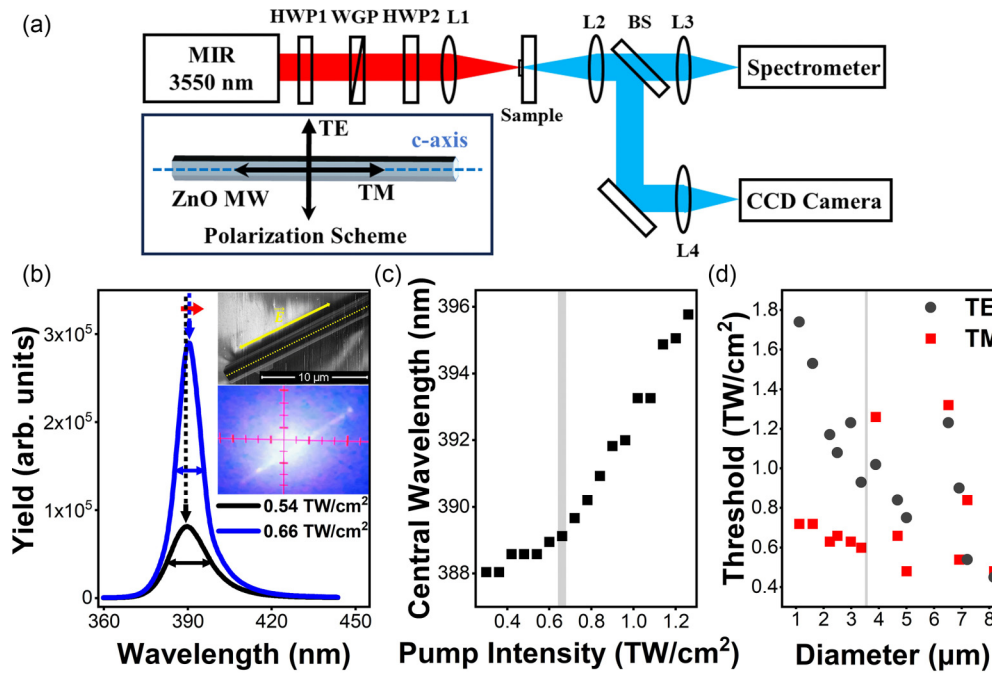
*cywu@pku.edu.cn

FIG. 1. Experimental setup and NUV emission spectrum of ZnO MW. (a) Experimental setup for MIR optical pumping and NUV detection. (b) NUV spectra below (black) and above (blue) lasing threshold. Inset: Top: incident polarization direction and SEM image of the pumped MW. Bottom: Optical image of the MW when pumped at 1.08 TW/cm^2. (c) Central wavelength of the NUV emission as a function of pump intensity. Gray box: lasing threshold. (d) TE and TM lasing threshold versus diameters of MWs. Gray box: pump laser wavelength.

exciton amplitudes. However, in the MIR-laser pumping case, electron-hole plasma (EHP), rather than excitons, forms the gain medium for lasing [19] because excitons do not exist at the MIR threshold intensity [26]. In addition, when pumped via UV light, most excited carriers are distributed near the surface owing to strong absorption, whereas in the MIR-laser pumping case, carriers are distributed inside the MW because ZnO is transparent to MIR light. The difference in carrier distribution may lead to a different lasing build-up process. Therefore, the similarity of the polarization dependence of MIR-pumped lasing to that of UV-pumped lasing is debatable, and research is still insufficient in this direction.

In this study, we experimentally measure the lasing of ZnO MW generated by intense MIR pulses and investigate its dependence on the polarization angle of the MIR pump laser. The diameters of the MWs are comparable to the pump wavelength, resulting in an intriguing diameter-related pump polarization dependence. By reproducing the observed phenomena via simulation, we confirm that the inhomogeneous carrier density distribution in the cross section, induced by the interference of pump light in the MW, and the absorption property of the ZnO MW, which is sensitive to defects and impurities in the sample, codetermine the polarization dependence. These findings highlight the feasibility of manipulation of ZnO MW lasing via geometry design and absorption property engineering, which paves the way for the practical application of MW in diverse research and industrial fields. In addition, customizing other incident-polarization-controlled microdevices may be feasible based on the same control mechanism.

The paper is organized as follows. In Sec. II, we present the measured ZnO MW lasing driven by MIR laser with different

polarizations. We found that the polarization dependence was ambiguous when the MW diameter was greater than the driving laser wavelength. In Sec. III, we propose a model to simulate the lasing processes in ZnO MW and reproduce the experimental observations. The ambiguous polarization dependence can be attributed to the optical interference of the driving laser and the various absorption properties of different MWs. Finally, a summary is given in Sec. IV.

II. EXPERIMENTAL RESULTS

Figure 1(a) shows the experimental setup and a schematic of the pump polarization notation. The ZnO MW samples used in the experiment were grown via chemical vapor deposition and transferred onto a fused silica substrate. The MWs were 1–10 μm in diameter and 100–500 μm in length. The 100-fs, 3.55-μm MIR pump light was linearly polarized and the power was adjusted through a combination of a half wave plate (HWP1) and a wire-grid polarizer (WGP). Subsequently, another half wave plate (HWP2) was used to adjust the pump polarization angle. Finally, the pump light was focused on the sample. Following pumping via the MIR laser, the ZnO MW emitted near-ultraviolet (NUV) light with a wavelength centered at approximately 390 nm, which was collected by a lens (L2) and divided into two beams using a beam splitter. One beam was measured via a spectrometer, and the other beam was imaged using an optical charge-coupled device (CCD), thereby enabling the simultaneous acquisition of the NUV spectrum and dark-field imaging of the ZnO MW sample. The polarization notation used in this paper is illustrated in the inset of Fig. 1(a): for the electric field of the pump laser $E \parallel c$ axis, the incident polarization is denoted as TM, and
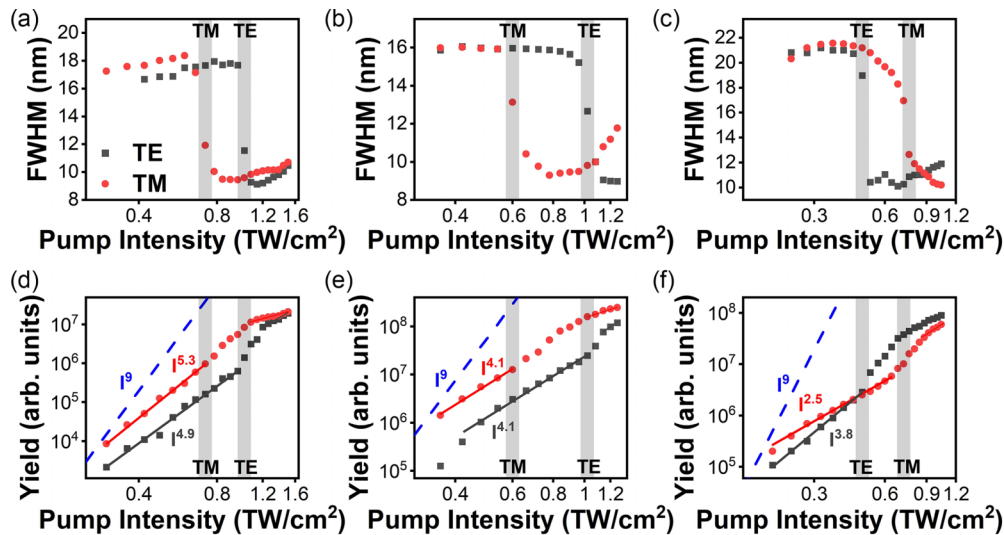
FIG. 2. Pump-laser-polarization dependent lasing threshold and NUV yield for MWs with different diameters. (a)–(c) FWHM, (d)–(f) NUV yield as a function of pump intensity for 2.5-μm (a), (d), 5.0-μm (b), (e), and 7.2-μm (c), (f) diameter MWs, respectively. Blue dashed line: Perturbative intensity scaling $\propto I^9$. Lasing thresholds for TE and TM polarized MIR laser are marked with gray boxes.

when $\boldsymbol{E} \perp c$ axis, the incident polarization is denoted as TE. The c axis is parallel to the axis of the MW.

Figure 1(b) shows the typical NUV emission spectra in the experiment and images of the corresponding MW [scanning electron microscopy (SEM) images (top) and optical images (bottom)]. A TM light was focused onto a ZnO MW with diameter $D = 5.0$ μm. With increase in pump intensity from 0.54 to 0.66 TW/cm², the intensity of NUV emission increased more than three times. This exhibits the nonlinear nature of MIR-laser excitation. The significant narrowing of the full width at half maximum (FWHM) of the NUV spectrum at high intensity indicates the occurrence of lasing. The lack of discrete lasing modes can be attributed to the absence of a homogeneous resonant cavity [27] resulting from the inhomogeneous excited carrier distribution (to be discussed later). As shown in the optical image, when pumped at 1.08 TW/cm², the most intensive collected lasing signal came from the pump focal region rather than from the ends of the MW, which was outside the direct excitation area. The optical image indicates strong light leakage from the side surface of the MW. This is different from the results of a previous study on ZnO NW lasing [19], wherein the waveguiding confinement of the NW side surface tends to cause the NW to emit light from both ends. This difference is attributed to both the micrometer-scale diameter and the strongly absorptive Urbach tail of our sample (to be discussed later). Figure 1(c) illustrates the pump intensity dependence of the NUV central wavelength for the same MW. The central wavelength remained unchanged until the lasing threshold was reached; later it monotonically red-shifted with the increase in the pump intensity, indicating that the gain medium of MW lasing formed via EHP, consistent with previous studies [19,22,28] as well as our carrier density calculation.

We prepared MW of different diameters and experimentally measured the dependence of ZnO MW lasing on the polarization angle of the pump field. Figure 2 shows the measured dependence of the FWHM and the yield of NUV emission on the pump intensity for TM- and TE-polarized

MIR lasers. The diameters of the targeted MWs are 2.5, 5.0, 7.2 μm from left to right. As evident from the upper panel, the FWHM demonstrates a significant narrowing at the lasing threshold, which is used as the marker for the lasing threshold. The relationship between the lasing thresholds for the TE ($I_{\text{th-TE}}$) and TM ($I_{\text{th-TM}}$) pump fields does not change monotonously with respect to the MW diameter. For the 2.5-μm diameter MW, which is below the pump wavelength, $I_{\text{th-TM}} < I_{\text{th-TE}}$ was observed. However, for MWs with diameters greater than the pump wavelength, $I_{\text{th-TM}} < I_{\text{th-TE}}$ for 5.0 μm and $I_{\text{th-TE}} < I_{\text{th-TM}}$ for 7.2 μm were observed. More evidence for this nontriviality is provided in Fig. 1(d), where $I_{\text{th-TM}} < I_{\text{th-TE}}$ was observed for all sub-pump-wavelength diameters (left), and no simple rules between $I_{\text{th-TM}}$ and $I_{\text{th-TE}}$ could be inferred for the above-pump-wavelength diameters (right).

In the lower panel of Fig. 2, the NUV yield versus the pump intensity demonstrates a clear transition from spontaneous emission to lasing emission [29]. The transition intensities coincide with the lasing thresholds shown in the upper panel. The NUV yields are normalized in the same manner for all MWs to render them quantitatively comparable. Regardless of the diameter or pump polarization, the intensity scaling of the NUV yield significantly deviates from the nine-photon perturbative power law ($E_{\text{gap}} \approx 9\hbar\omega_{\text{MIR}}$), reflecting the nonperturbative tunneling nature of MIR-laser-pumped lasing: At high intensity, the light field bends the potential, enabling the electron to tunnel from valence band to conduction band. This leads to a carrier excitation rate that scales with intensity more like a field-driven law than a multiphoton perturbative law [30]. The TM-polarized MIR light generated a higher NUV yield for all diameters when the pump intensity was below the lasing threshold. However, when the pump intensity exceeded the lasing threshold, the lasing yield exhibited a polarization-dependent efficiency similar to that of the lasing threshold for the respective MWs. For 2.5- and 5.0-μm-diameter MWs, the lasing yield was higher when pumped with TM laser, whereas the TE pumped lasing yield was higher for the
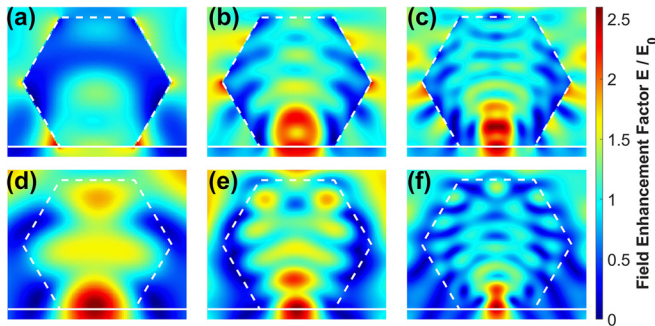
FIG. 3. FDTD simulation for MIR field distribution in the cross sections of MWs with different diameters. Normalization to the incident field strength is performed. Interference patterns generated by TE (a)–(c) and TM (d)–(f) polarized laser are demonstrated, wherein MW diameters are 2.5 μm (a), (d), 5.0 μm (b), (e), and 7.2 μm (c), (f), respectively. White hexagonal dashed lines and straight solid lines illustrate the side surface of the MW and the upper surface of the substrate, for eye's guidance.

7.2-μm-diameter MW. The experimental results for the lasing threshold and intensity contradict the normal expectation for NW lasing that the TM pump is more efficient for lasing [31], indicating the complicated process involved in lasing with an increase in the dimensions. Analytically, the TE polarized light attenuates as $E_{inside} = 2\varepsilon_0/(\varepsilon + \varepsilon_0) E_{vacuum}$ inside the NW, where ε_0 and ε are dielectric functions of the vacuum and the material, whereas TM light maintains incident intensity [31]. Therefore, TM light is more efficient for pumping NW lasing. As the diameter of the wire exceeds pump wavelength (>3.55 μm), far above the lasing wavelength (≫390 nm), the MIR laser may generate a polarization dependent complicated interference pattern in the MW, which may modulate gain and loss competition in the build-up process of lasing.

III. SIMULATION AND DISCUSSION

To model the polarization dependence of lasing in the ZnO MW, we first perform finite difference time domain (FDTD) simulations on the MWs. According to the optical image, the collected lasing signal mostly originated from the focus area, indicating that end-facet waveguiding lasing did not dominate, so the MW could be considered symmetric along the *c* axis. Therefore, calculating the light field distribution in the cross section provides sufficient information for modeling [20]. The simulative pump field distribution in the cross sections of MWs with diameters 2.5, 5.0, and 7.2 μm are shown in Fig. 3. The field distribution is demonstrated by the distribution of field enhancement factor (FEF) $|\mathbf{E}(\mathbf{r})/\mathbf{E}_0|$, wherein $\mathbf{E}(\mathbf{r})$ is the field strength at position $\mathbf{r}$ and $\mathbf{E}_0$ is the vacuum field strength. The upper and lower panels correspond to the TE and TM polarizations, respectively. At first sight, significant interference pattern of the pump field appears for all diameters, which is in sharp contrast to the NW pumped by the above-bandgap photons, wherein no interference occurs inside the NW owing to strong absorption. The interference pattern results in a spatially nonuniform carrier distribution and, thus, an inhomogeneous refractive-index distribution [20]. A number of resonant modes are supported by such inhomogeneity,

resulting in continuous lasing spectrum formed by their spectral overlap [26] [0.66 TW/cm² spectrum in Fig. 1(b)]. For 2.5-μm-diameter MW whose diameter is smaller than the pump wavelength, mesoscopic selection on TM polarization occurs, similar to the NW case. In Figs. 3(a) and 3(d), the TE field attenuates inside the MW, whereas the TM field constructively interferes, rendering the TM field more efficient for lasing. This is consistent with the experimental results and the normal expectation. For MWs with above-pump-wavelength diameters, as shown in Figs. 3(b), 3(c), 3(e), and 3(f), the maximum FEF is slightly higher when the MW is pumped by TM light than when it was pumped by TE light. However, the area with constructive interference (FEF > 1) is considerably larger in the TE case than in the TM case. The similarity of the interference patterns for MWs with above-wavelength diameters indicates that interference enhancement alone is insufficient to explain the observed polarization dependence of lasing threshold. The absorption rate of the sample, which is directly related to the round-trip net gain in the lasing built-up process, should be considered in detail.

To investigate the influence of the optical properties of ZnO on MW lasing, we reproduce the experimental results for MWs with the aforementioned wavelength diameters by thoroughly modeling the lasing process based on the *in situ* characterization of the sample. In our model, the MW lasing process is decomposed into three steps: carrier injection via MIR laser pumping, EHP gain medium formation, and lasing emission, as schematically shown in Fig. 4(a). Electrons and holes are first excited via strong-field tunneling and then evolve to form EHP gain medium. Finally, the optical gain induced by the propagation in the EHP gain medium resulted in MW lasing when the round-trip gain exceeds the loss. The pulse width of the MIR light used in the experiment is 100 fs, which was considerably shorter than the typical timescale for EHP formation (approximately 1 ps) [10,32]. Therefore, ultrafast excitation step 1 and gain medium formation step 2 are temporally decoupled and can be calculated sequentially. This decoupling is experimentally supported by the pump-intensity dependence of the fifth harmonic [Fig. 4(b)]. The fifth harmonic, which is generated only in the presence of the MIR laser, exhibits no transition at the lasing threshold, indicating that the gain medium is formed afterward and does not affect the carrier injection step 1. Notably, a stronger fifth harmonic is generated by the TM light in both MWs, which is consistent with the FDTD result that a higher FEF is achieved by the TM light.

For carrier injection step 1, Figs. 2(d)–2(f) show the nonperturbative nature of MIR pumping. Moreover, the Keldysh parameter for the pump intensity used in the experiment was in the range 0.45–1.00. Therefore, the carrier injection rate is calculated using the Keldysh tunneling theory combined with impact ionization [19,30], with the effective mass taken from the literature [33]. The calculation shows that carrier density at lasing threshold is higher than 1.2×10^{25} m⁻³, which exceeds the Mott density (1.5×10^{24} m⁻³) [26], thereby confirming the EHP nature of ZnO MW lasing at room temperature [22]. Owing to the transparency of ZnO in the MIR spectral range, the interference pattern in the MW can be directly mapped into an inhomogeneous carrier excitation density distribution, which further translates into the gain property in step 2.
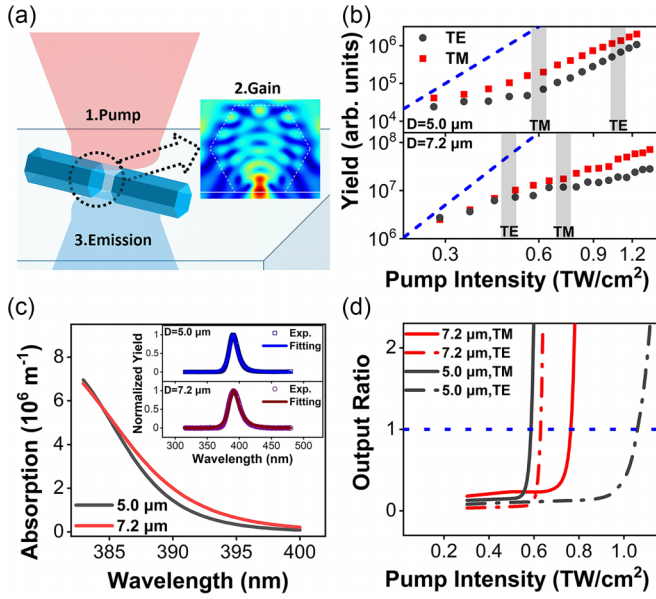
FIG. 4. Analysis of pump-laser-polarization dependent lasing in ZnO MW with diameter greater than pump wavelength. (a) Schematics for the build-up process of lasing in MW. (b) Measured fifth harmonic versus pump intensity for 5.0-μm (upper) and 7.2-μm (lower) diameter MW. Blue dashed line: Perturbative harmonic intensity scaling $\propto I^5$. (c) Calculated absorption curve in the NUV emission spectral range for the 5.0-μm and 7.2-μm diameter MW. Inset: comparison between experimental and fitting NUV spectra for 5.0-μm (upper) and 7.2-μm-diameter MW (lower), when pumped at 0.36 TW/cm^2. (d) Simulation result for NUV output ratio versus pump intensity for 7.2-μm (red) and 5.0-μm (dark gray) diameter MW when being pumped by TM (solid) and TE (dash-dotted) polarized MIR laser. Intersections with unity (blue dotted line) denote lasing threshold.

In step 2, the absorption curve immediately below the band gap, called the Urbach tail [34], exerts a direct influence on lasing. A longer Urbach tail broadens the bandwidth of the NUV emission because more optical transitions are allowed at longer wavelengths. As a result, lower carrier density is required to achieve the same gain rate in the NUV emission spectral range. Therefore, a longer tail renders the TM polarization more efficient for lasing because of its higher maximum FEF to achieve higher gain rate. However, a longer tail may also lower the round-trip net gain owing to the increase in absorption rate in the unexcited region. The area with constructive interference is considerably larger in the TE case than in the TM case (Fig. 3), rendering TM polarization less efficient for lasing. To evaluate the competition between these two effects, the curves of the absorption (gain) rate of the sample are calculated based on the Bethe-Salpeter ladder equation (BSE), wherein a phenomenological imaginary part of the susceptibility is utilized to describe the Urbach tail, as proposed in the literature [20],

$$\gamma(\omega) = \frac{\gamma_0}{1 + \exp\left(\frac{-\hbar\omega + E_G - E_s}{E_u} - 1\right)}, \qquad (1)$$

where $\hbar\omega$, E_G, and E_S are photon energy and carrier density dependent band-gap and exciton binding energy, respectively,

and E_u and γ_0 are the fitting parameters, where the former one is the Urbach energy and the latter is the magnitude of the tail. The Urbach tail originates from impurities and defects in the sample [35], hence it is sensitive to the growth conditions and varies from point to point on the sample. Only *in situ* characterization provides a reliable explanation of the relative phenomena. To obtain the correct parameters for $\gamma(\omega)$, the experimentally measured NUV spectra are fitted to the calculated spectrum based on BSE. When the pump intensity is below the lasing threshold, the spatially inhomogeneous effects arising from the carrier density distribution that may influence the NUV emission spectrum, including the nonuniform renormalized band gap, refractive index, and absorption rate, are negligible. This renders the NUV spectrum under this condition particularly suitable for *in situ* characterization of the intrinsic absorption curve. For this pump intensity, the NUV spectrum is linked to the absorption curve using the extended Roosbroeck-Shockley relation [36,37]:

$$I_{\mathrm{PL}}(\hbar\omega) = A_{\mathrm{norm}} \frac{(\hbar\omega)^2 \{1 - \exp\left[-\alpha(\hbar\omega)d_{\mathrm{eff}}\right]\}}{\exp\left(\frac{\hbar\omega}{k_{\mathrm{B}}T_{\mathrm{e}}}\right) - 1}, \qquad (2)$$

where $\hbar\omega$ is the photon energy, A_{norm} is the normalized factor, effective absorption depth d_{eff} and thermal electron temperature T_e are valued within the neighborhood range of the bulk sample [36,37], and the absorption curve $\alpha(\hbar\omega)$ is calculated from BSE and is dependent on parameters E_u and γ_0. The best fit provides the parameters for E_u and γ_0, generating the carrier density dependent absorption (gain) curve for each MW. A negative absorption rate implies a positive gain rate in this theory. Figure 4(c) illustrates the calculated intrinsic absorption curve in the NUV emission spectral range for MWs with diameters 7.2 and 5.0 μm, where the Urbach tail is longer and clearly more absorptive for the 7.2-μm MW. A comparison between the normalized experimental and fitted spectra for the two MWs exhibits good agreement, as shown in the inset. By combining the calculated absorption (gain) curve with the Keldysh excitation rate and FDTD results (Fig. 3), the gain medium distribution of step 2 can be obtained for each pump intensity. Using the transient grating technique, the diffusion coefficient has been measured to be 3 cm^2/s at a carrier excitation density of 10^{26} m^{-3} in ZnO [38]. Consequently, at threshold intensity, the estimated diffusion length is less than 5 nm at the lasing emission moment [39]. Because the diffusion length is orders of magnitude shorter than lasing wavelength and the lateral dimension of constructive interference area, the impact of carrier diffusion on the gain distribution is neglected in our simulation.

In step 3, lasing emission builds up in the feedback cavity. A waveguiding Fabry-Perot (FP) cavity made of end facets is excluded because of the nondominance of end emission in Fig. 1(b), supported by the strong absorptive property shown in Fig. 4(c). As the length of the MW exceeds the diameter of the focus, the strong absorption lowers the net gain for end-facet lasing and increases the lasing threshold. In Fig. 3, the inhomogeneous carrier distribution in the cross section dynamically modifies the refractive index distribution, resulting in the broadening of the lasing modes and strong leaking features of the whispering gallery cavity. Therefore, an FP cavity comprising two side surfaces in the direction of the

incident light is proposed as the feedback cavity. The round-trip total flux for light emission at 390 nm, approximately the central lasing wavelength at threshold intensity, is calculated. The flux is proportional to $\oint_{\text{roundtrip}} N(\mathbf{r})\{\exp[g(\mathbf{r})]\}d|\mathbf{r}|$, where $N(\mathbf{r})$ is the carrier density at position $\mathbf{r}$, and $g(\mathbf{r})$ is the carrier density dependent gain coefficient at position $\mathbf{r}$. The photon flux increases with each round trip when the gain exceeds loss, resulting in higher flux at 390 nm compared to other wavelengths and eventually linewidth narrowing in the total emission spectrum. Figure 4(d) illustrates the calculated output intensity ratio, defined as the ratio of the total gained NUV flux at 390 nm in an optically excited MW to that in a lossless MW of the same size, for different pump intensity and laser polarization. The intersection of output ratio with the unity output ratio is defined as the lasing threshold because the NUV line shape changes drastically with further increase in the pump intensity. The simulated relative NUV yield is manifested by the relative heights of the curves. The threshold relations $I_{\text{th-TM}} < I_{\text{th-TE}}$ for 5.0 μm and $I_{\text{th-TE}} < I_{\text{th-TM}}$ for 7.2 μm MW are reproduced via simulation. In addition, the NUV yield relations are also well reproduced: TM light generates stronger lasing intensity in the 5.0-μm MW, whereas the TE field generates stronger lasing intensity in the 7.2-μm MW. If the pump intensity is below the lasing threshold, the NUV yield favors TM polarization in both MWs owing to its higher maximum FEF. The good agreement between the simulation and experimental results confirms the gain and loss competition mechanism for polarization-dependent lasing, wherein the pump field interference pattern and absorption properties of the ZnO sample jointly regulate the round-trip net gain in MW.

IV. CONCLUSION

We investigated the size-related dependence of ZnO MW lasing on the polarization of intense MIR pumping laser. The TM-polarized light generated a lower lasing threshold and higher yield in the MW with a sub-pump-wavelength diameter, as expected. However, in MWs with diameters greater than the pump wavelength, lasing efficiency was not solely determined by pump polarization. Instead, the polarization dependence was sensitive to the *in situ* absorption properties of the specific sample, as confirmed by our simulation. For MW with wider NUV bandwidth (longer Urbach tail), the TE field might be more efficient for lasing. The polarization dependence is thus confirmed in this study to be determined by the absorption properties of the sample and the pump interference pattern in the MW. The former is sensitive to impurities or defect concentrations in the sample introduced during the growth process, whereas the latter is geometrically related to the ratio of the diameter to the pump wavelength, as evident from the FDTD calculation. Considering that NW lasing exhibits pump wavelength independence in the MIR range [19], our findings are generally applicable to a wide wavelength range, as optically excited MW amount to a bundle of NW with different excited degrees, which paves the way for versatile applications, including MW-based polarization-sensitive self-powered microphotodetectors [40], on-chip photonic logical elements, and biological selective microlasing. A novel exploration of how different types and concentrations of impurities or defects change the polarization dependence of MIR-pumped MW via Urbach tail engineering [35,41] might be worthwhile, as the importance of the intrinsic absorption properties of the sample is emphasized in this paper. Similar research on other 1D microstructures, such as AlN microstructures (band gap of approximately 6.2 eV [42]) used as a deep-ultraviolet microlaser, may be beneficial for extending the application range of the proposed lasing-controlled mechanism.

[1] S. Choi and I. Aharonovich, Zinc oxide nanophotonics, Nanophotonics **4**, 437 (2015).

[2] C. Xu, J. Dai, G. Zhu, G. Zhu, Y. Lin, J. Li, and Z. Shi, Whispering-gallery mode lasing in ZnO microcavities, Laser Photon. Rev. **8**, 469 (2014).

[3] D. Vanmaekelbergh and L. K. van Vugt, ZnO nanowire lasers, Nanoscale **3**, 2783 (2011).

[4] D. C. Reynolds, D. C. Look, and B. Jogai, Optically pumped ultraviolet lasing from ZnO, Solid State Commun. **99**, 873 (1996).

[5] C. Czekalla, C. Sturm, R. Schmidt-Grund, B. Cao, M. Lorenz, and M. Grundmann, Whispering gallery mode lasing in zinc oxide microwires, Appl. Phys. Lett. **92**, 241102 (2008).

[6] J. C. Johnson, H. Yan, P. Yang, and R. J. Saykally, Optical cavity effects in ZnO nanowire lasers and waveguides, J. Phys. Chem. B **107**, 8816 (2003).

[7] L. Sun, Z. Chen, Q. Ren, K. Yu, L. Bai, W. Zhou, H. Xiong, Z. Q. Zhu, and X. Shen, Direct observation of whispering gallery mode polaritons and their dispersion in a ZnO tapered microcavity, Phys. Rev. Lett. **100**, 156403 (2008).

[8] S. Choi, B. C. Johnson, S. Castelletto, C. Ton-That, M. R. Phillips, and I. Aharonovich, Single photon emission from ZnO nanoparticles, Appl. Phys. Lett. **104**, 261101 (2014).

[9] J. Dai, C. Xu, T. Nakamura, Y. Wang, J. Li, and Y. Lin, Electron-hole plasma induced band gap renormalization in ZnO microlaser cavities, Opt. Express **22**, 28831 (2014).

[10] M. Wille, C. Sturm, T. Michalsky, R. Roder, C. Ronning, R. Schmidt-Grund, and M. Grundmann, Carrier density driven lasing dynamics in ZnO nanowires, Nanotechnology **27**, 225702 (2016).

[11] S. Shekhar, W. Bogaerts, L. Chrostowski, J. E. Bowers, M. Hochberg, R. Soref, and B. J. Shastri, Roadmapping the next generation of silicon photonics, Nat. Commun. **15**, 751 (2024).

[12] C. P. Dietrich, A. Fiore, M. G. Thompson, M. Kamp, and S. Höfling, GaAs integrated quantum photonics: Towards compact and multi-functional quantum photonic integrated circuits, Laser Photon. Rev. **10**, 870 (2016).

[13] R. Nagarajan, M. Kato, J. Pleumeekers, P. Evans, S. Corzine, S. Hurtt, A. Dentai, S. Murthy, M. Missey, R. Muthiah *et al.*, InP photonic integrated circuits, IEEE J. Sel. Top. Quantum Electron. **16**, 1113 (2010).

[14] C. Zhang, F. Zhang, T. Xia, N. Kumar, J.-I. Hahm, J. Liu, Z. L. Wang, and J. Xu, Low-threshold two-photon pumped ZnO nanowire lasers, Opt. Express **17**, 7893 (2009).

[15] J. Dai, Q.-F. Dai, J.-H. Zeng, S. Lan, X. Wan, and S.-L. Tie, Negative slope for second harmonic generation observed at high excitation intensities in ZnO nanorods, IEEE J. Quantum Electron. **49**, 903 (2013).

[16] C. F. Zhang, Z. W. Dong, G. J. You, S. X. Qian, and H. Deng, Multiphoton route to ZnO nanowire lasers, Opt. Lett. **31**, 3345 (2006).

[17] K. Han, J. Wang, Y. Sheng, F. Ju, X. Sheng, Y. Wu, and G. Tang, Multi-photon-pumped stimulated emission from ZnO nanowires: A time-resolved study, Phys. Lett. A **376**, 1871 (2012).

[18] A. Chen, H. Zhu, Y. Wu, D. Yang, J. Li, S. Yu, Z. Chen, Y. Ren, X. Gui, S. Wang *et al.*, Low-threshold whispering-gallery mode upconversion lasing via simultaneous six-photon absorption, Adv. Opt. Mater. **6**, 1800407 (2018).

[19] R. Hollinger, P. Malevich, V. Shumakova, S. Ališauskas, M. Zapf, R. Röder, A. Pugžlys, A. Baltuška, C. Ronning, C. Spielmann *et al.*, Strong light-field driven nanolasers, Nano Lett. **19**, 3563 (2019).

[20] Y. Liang, H. Zhu, H. Zheng, Z. Tang, Y. Wang, H. Wei, R. Hong, X. Gui, and Y. Shen, Competition of whispering gallery lasing modes in microwire with hexagonal cavity, J. Phys. D: Appl. Phys. **54**, 055107 (2021).

[21] T. Michalsky, M. Wille, M. Grundmann, and R. Schmidt-Grund, Tunable and switchable lasing in a ZnO microwire cavity at room temperature, J. Phys. D: Appl. Phys. **51**, 425305 (2018).

[22] M. A. M. Versteegh, D. Vanmaekelbergh, and J. I. Dijkhuis, Room-temperature laser emission of ZnO nanowires explained by many-body theory, Phys. Rev. Lett. **108**, 157402 (2012).

[23] T. P. H. Sidiropoulos, R. Röder, S. Geburt, O. Hess, S. A. Maier, C. Ronning, and R. F. Oulton, Ultrafast plasmonic nanowire lasers near the surface plasmon frequency, Nat. Phys. **10**, 870 (2014).

[24] Y. Wang, Y. Liu, P. Jiang, Y. Gao, H. Yang, L.-Y. Peng, Q. Gong, and C. Wu, Optical switch of electron-hole and electron-electron collisions in semiconductors, Phys. Rev. B **107**, L161301 (2023).

[25] Z. Ye, F. Chen, H. Zhou, S. Luo, F. Sun, Z. Sun, Y. Zheng, X. Chen, H. Xu, Z. Chen *et al.*, Excitation-polarization-dependent dynamics of polariton condensates in the ZnO microwire at room temperature, J. Phys.: Condens. Matter **34**, 22LT01 (2022).

[26] M. A. M. Versteegh, T. Kuis, H. T. C. Stoof, and J. I. Dijkhuis, Ultrafast screening and carrier dynamics in ZnO: Theory and experiment, Phys. Rev. B **84**, 035207 (2011).

[27] H. Cao, Lasing in random media, Waves Random Complex Media **13**, R1 (2003).

[28] R. Hollinger, E. Haddad, M. Zapf, V. Shumakova, P. Herrmann, R. Röder, I. Uschmann, U. Reislöhner, A. Pugžlys, A. Baltuška *et al.*, Role of free-carrier interaction in strong-field excitations in semiconductors, Phys. Rev. B **104**, 035203 (2021).

[29] M. A. Zimmler, J. Bao, F. Capasso, S. Müller, and C. Ronning, Laser action in nanowires: Observation of the transition from amplified spontaneous emission to laser oscillation, Appl. Phys. Lett. **93**, 051101 (2008).

[30] L. V. Keldysh, Ionization in the field of a strong electromagnetic wave, Sov. Phys. JETP **20**, 1307 (1965).

[31] J. Wang, M. S. Gudiksen, X. Duan, Y. Cui, and C. M. Lieber, Highly polarized photoluminescence and photodetection from single indium phosphide nanowires, Science **293**, 1455 (2001).

[32] E. Hendry, M. Koeberg, and M. Bonn, Exciton and electron-hole plasma formation dynamics in ZnO, Phys. Rev. B **76**, 045214 (2007).

[33] K. J. Button, D. R. Cohn, M. von Ortenbert, B. Lax, E. Mollwo, and R. Helbig, Zeeman splitting of anomalous shallow bound states in ZnO, Phys. Rev. Lett. **28**, 1637 (1972).

[34] F. Urbach, The long-wavelength edge of photographic sensitivity and of the electronic absorption of solids, Phys. Rev. **92**, 1324 (1953).

[35] J. D. Dow and D. Redfield, Toward a unified theory of Urbach's rule and exponential absorption edges, Phys. Rev. B **5**, 594 (1972).

[36] B. Ullrich, S. Yano, R. Schroeder, and H. Sakai, Analysis of single- and two-photon-excited green emission spectra of thin-film cadmium sulfide, J. Appl. Phys. **93**, 1914 (2003).

[37] B. Ullrich, A. K. Singh, M. Bhowmick, P. Barik, D. Ariza-Flores, H. Xi, and J. W. Tomm, Photoluminescence lineshape of ZnO, AIP Adv. **4**, 123001 (2014).

[38] P. Onufrijevs, P. Ščajev, K. Jarašiūnas, A. Medvid, V. Korsaks, N. Mironova-Ulmane, M. Zubkins, and H. Mimura, Photo-electrical and transport properties of hydrothermal ZnO, J. Appl. Phys. **119**, 135705 (2016).

[39] A. Block, M. Liebel, R. Yu, M. Spector, Y. Sivan, F. J. Garcia de Abajo, and N. F. van Hulst, Tracking ultrafast hot-electron diffusion in space and time by ultrafast thermomodulation microscopy, Sci. Adv. **5**, eaav8965 (2019).

[40] Z.-D. Shui, S. Wang, Z. Yang, D. Wang, B.-Z. Tian, S. Luo, Z. Wang, and L. Yang, Polarization-sensitive self-powered tellurium microwire near-infrared photodetector, Appl. Phys. Lett. **122**, 101902 (2023).

[41] R. C. Rai, Analysis of the Urbach tails in absorption spectra of undoped ZnO thin films, J. Appl. Phys. **113**, 153508 (2013).

[42] M. H. Wong, O. Bierwagen, R. J. Kaplar, and H. Umezawa, Ultrawide-bandgap semiconductors: An overview, J. Mater. Res. **36**, 4601 (2021).